nature photonics

SUPPLEMENTARY INFORMATION
https://doi.org/10.1038/s41566-019-0526-z

In the format provided by the authors and unedited.

Efficient colloidal quantum dot light-emitting diodes operating in the second near-infrared biological window

Maria Vasilopoulou[1]*, Hyeong Pil Kim[2], Byung Soon Kim[2], Michael Papadakis[3], Anderson Emanuel Ximim Gavim[4], Andreia Gerniski Macedo[5], Wilson Jose da Silva[5], Fabio Kurt Schneider[5], Mohd Asri Mat Teridi[6], Athanassios G. Coutsolelos[3]* and Abd. Rashid bin Mohd Yusoff[2,7]*

[1]Institute of Nanoscience and Nanotechnology, National Center for Scientific Research "Demokritos", Attica, Greece. [2]Advanced Display Research Center, Department of Information Display, Kyung Hee University, Seoul, South Korea. [3]Department of Chemistry, University of Crete, Laboratory of Bioinorganic Chemistry, Crete, Greece. [4]Universidade Tecnológica Federal do Parana, CPGEI, Curitiba, Paraná, Brazil. [5]Universidade Tecnológica Federal do Parana, PPGFA, Curitiba, Paraná, Brazil. [6]Solar Energy Research Institute, National University of Malaysia, Selangor, Malaysia. [7]Department of Physics, Swansea University, Swansea, UK. *e-mail: m.vasilopoulou@inn.demokritos.gr; acoutsol@uoc.gr; a.r.mohdyusoff@swansea.ac.uk

Supplementary Figures

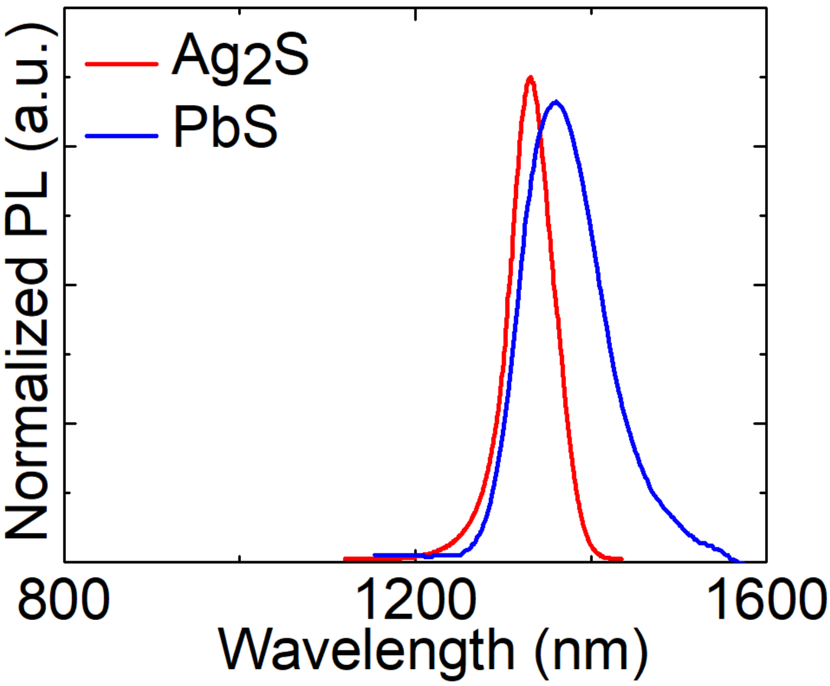

Supplementary Fig. 1 PL comparison. Steady-state photoluminescence (PL) spectra of Ag_2S and PbS CQDs. A smaller FWHM is clearly observed for Ag_2S indicating higher colour purity compared to PbS.

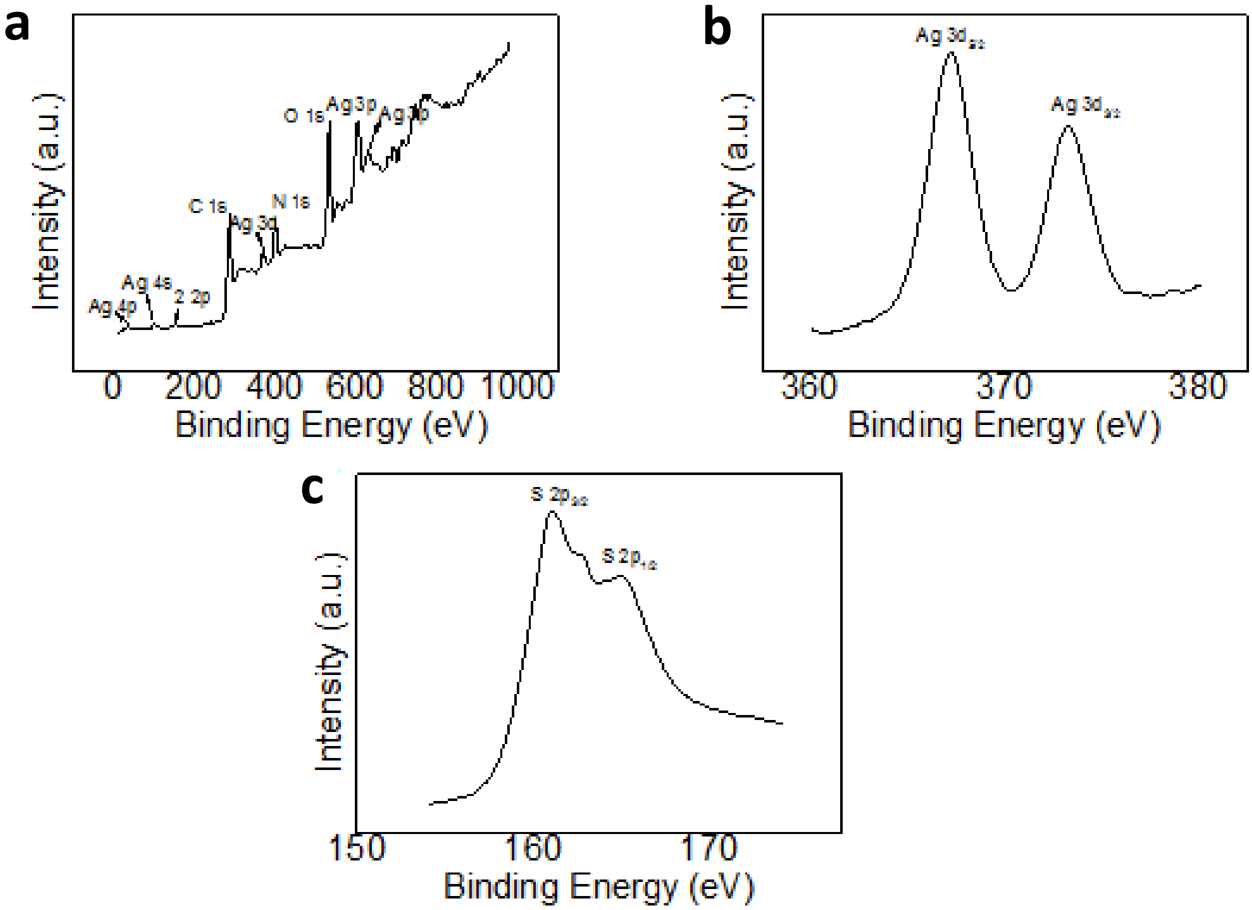

Supplementary Figure 2 Compositional study of Ag_2S CQDs. XPS spectra of the pure CQDs: **a**, the whole survey and **b**, Ag 3d and **c**, S 2p core levels. The Ag 3d XPS core levels consist of two peaks at binding energies (BEs) of 368.2 and 374.3 eV, which can be assigned to Ag $3d_{5/2}$ and Ag $3d_{3/2}$ of the Ag^+ ions in the Ag_2S CQDs[1]. In the XPS S 2p core level, the peaks located at BEs of 161.3 and 162.5 eV can be assigned to S $2p_{3/2}$ and S $2p_{1/2}$ of the S^{2-} in the Ag_2S CQDs[1]. No Ag and S atoms of other oxidation states were detected.

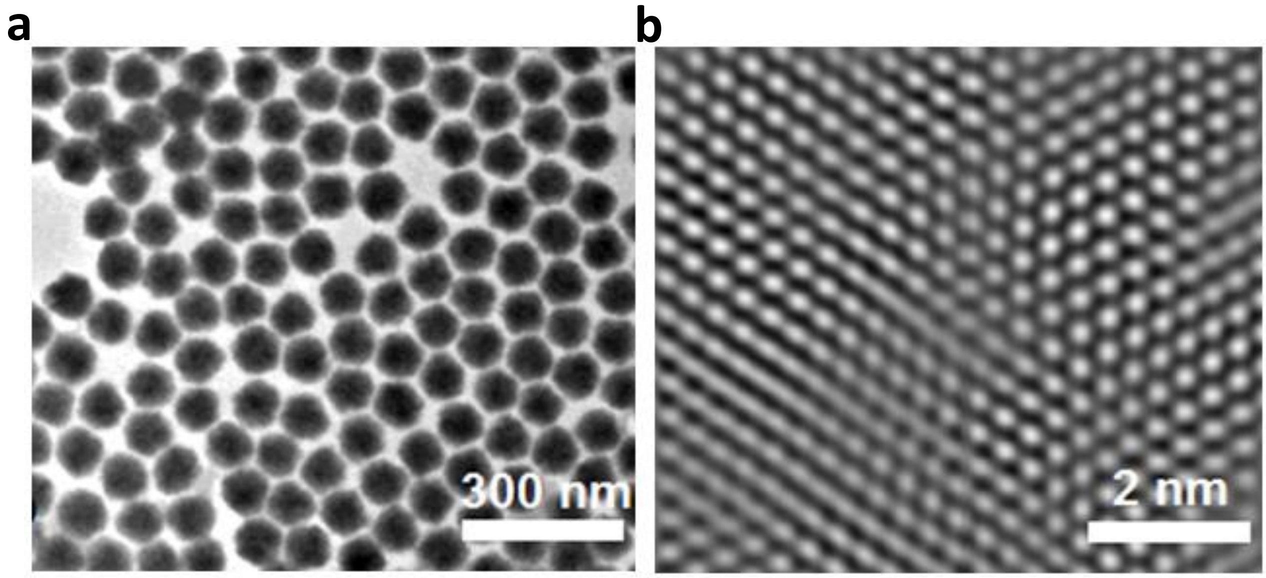

Supplementary Figure 3 Morphological properties of CQDs. a, TEM image of CQDs, and **b**, fast-Fourier transform (FFT)-HRTEM image of CQDs. The as-prepared Ag_2S CQDs were highly dispersed, with a two-dimensional ordered arrangement. The HRTEM image indicates that the CQDs were single crystalline.

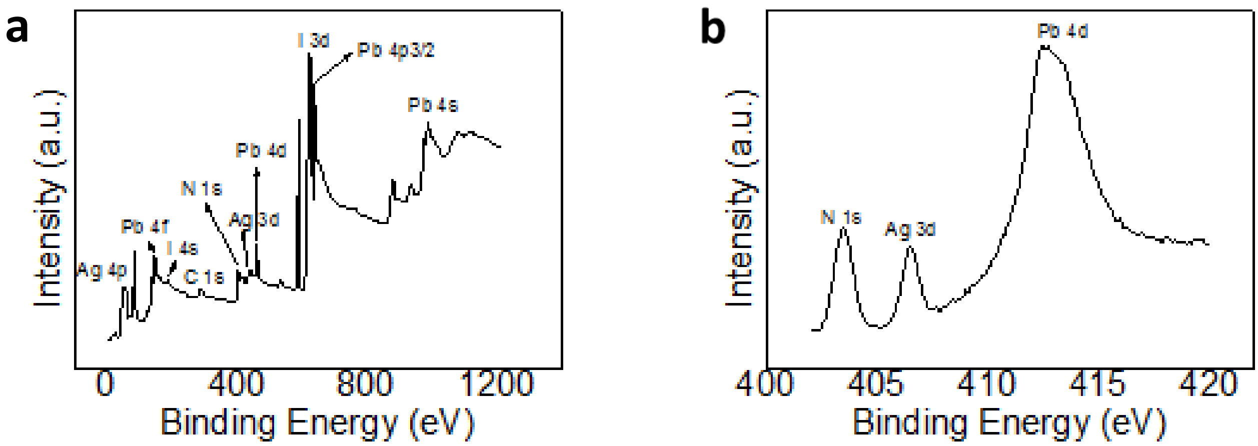

Supplementary Figure 4 Compositional study of CQDs in the perovskite. XPS spectra of the CQDs in the triple cation ($Cs_{10}(MA_{0.17}FA_{0.83})Pb(Br_xI_{1-x})_3$) perovskite: **a**, the whole survey and **b**, Ag 3d, Pb 4d and N 1s core levels. The XPS high-resolution spectra involving Ag 3d, Pb 4d, and N 1s verified the existence of Ag_2S CQD dopants in the host perovskite matrix[2].

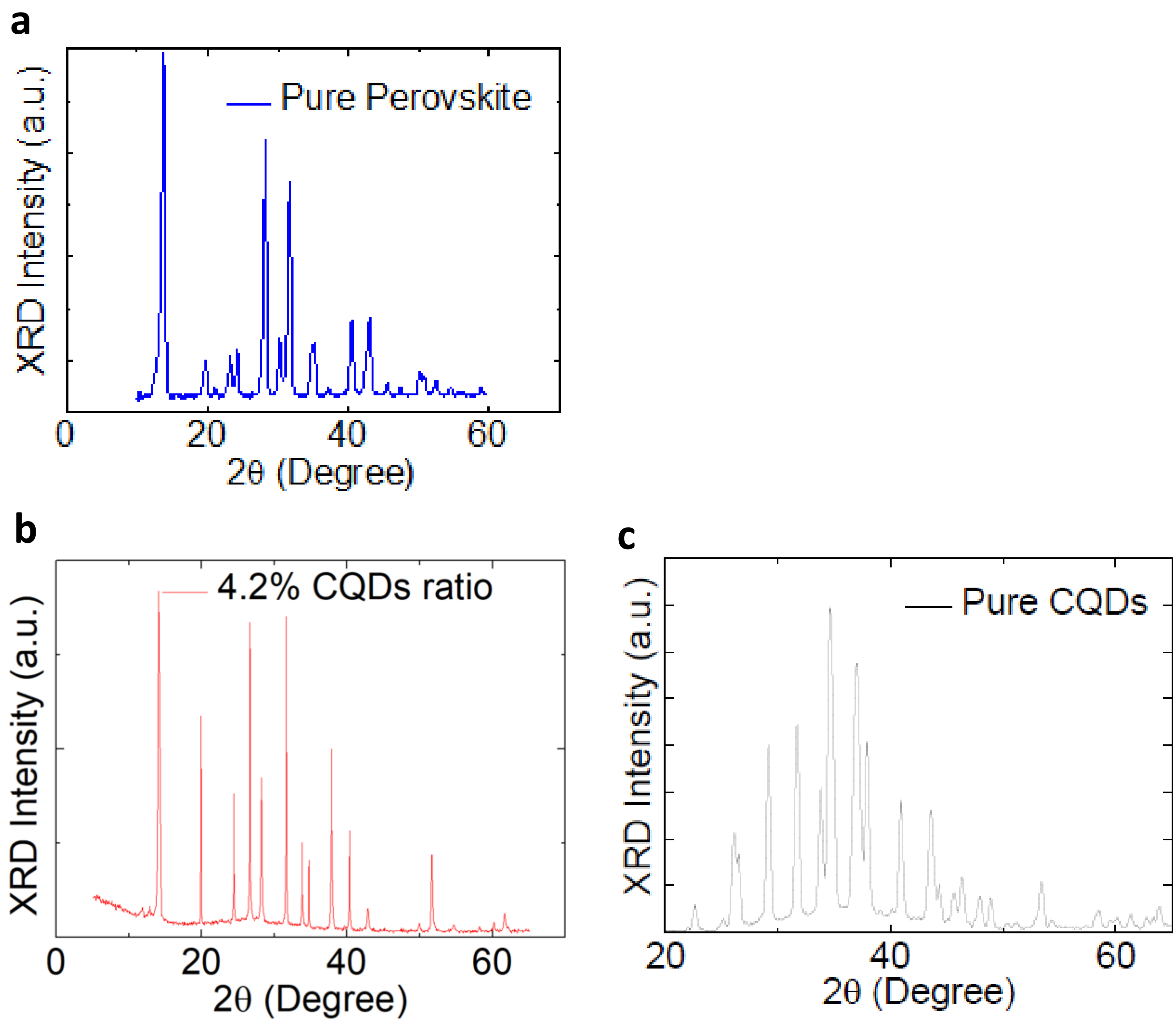

Supplementary Figure 5 Crystal structure characterization. XRD patterns of the **a**, triple cation perovskite, **b**, CQDs in the triple cation perovskite and **c**, pure CQDs. In the XRD pattern of the pure perovskite, the typical perovskite peak at ~14° is evident[3]. In the XRD patterns of the pure CQDs, the peaks match those of monoclinic Ag_2S (JCPDS 14-0072)[4]. The broadening of the diffraction peaks suggests the nanocrystalline nature of the CQDs.

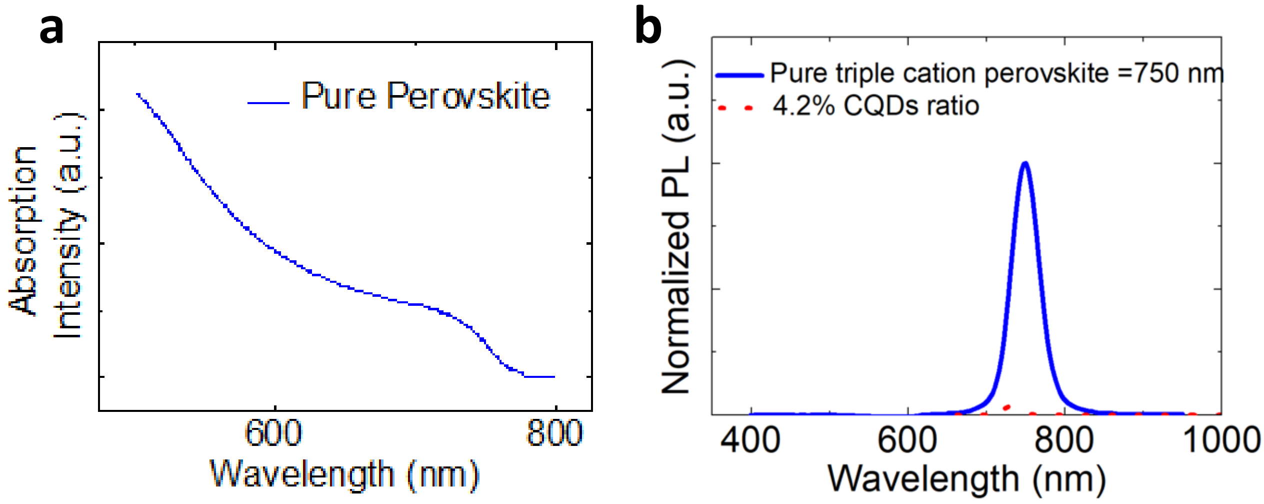

Supplementary Figure 6 Optoelectronic properties of mixed cation perovskite film. **a**, Absorption spectrum of the pure perovskite, and **b**, steady-state PL spectrum of the pure perovskite with peak emission at 750 nm and after embedding CQDs resulting to quenching of PL. The latter spectrum indicates effective energy transfer from the perovskite matrix to CQD emitters.

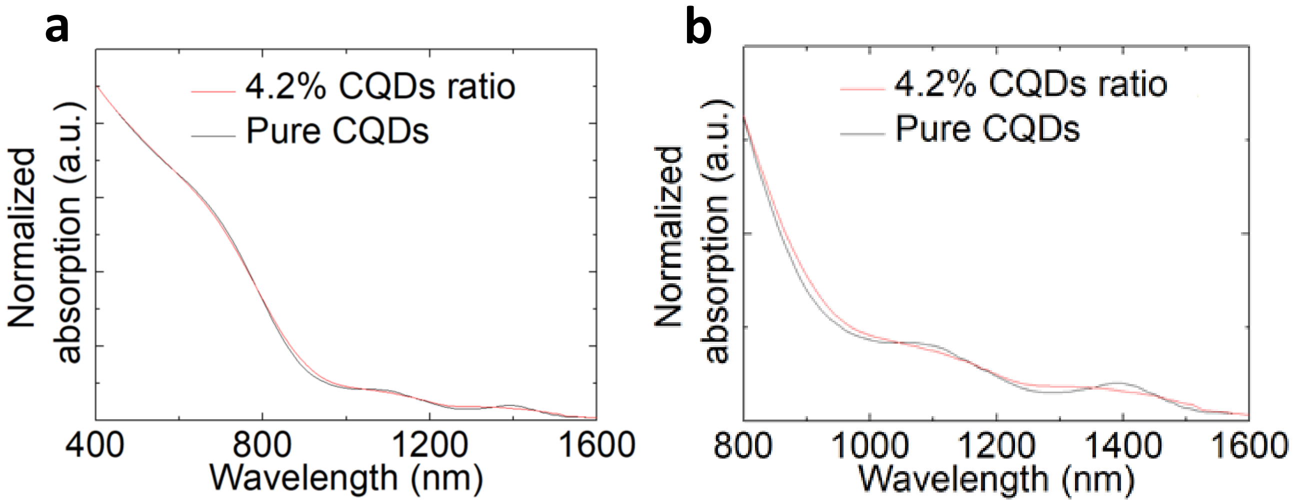

Supplementary Figure 7 UV-Vis absorption measurements. a, Absorption spectra of pure CQDs and CQDs in the triple cation perovskite. **b,** Magnification of the absorption onset region for the estimation of the optical bandgap of CQDs film.

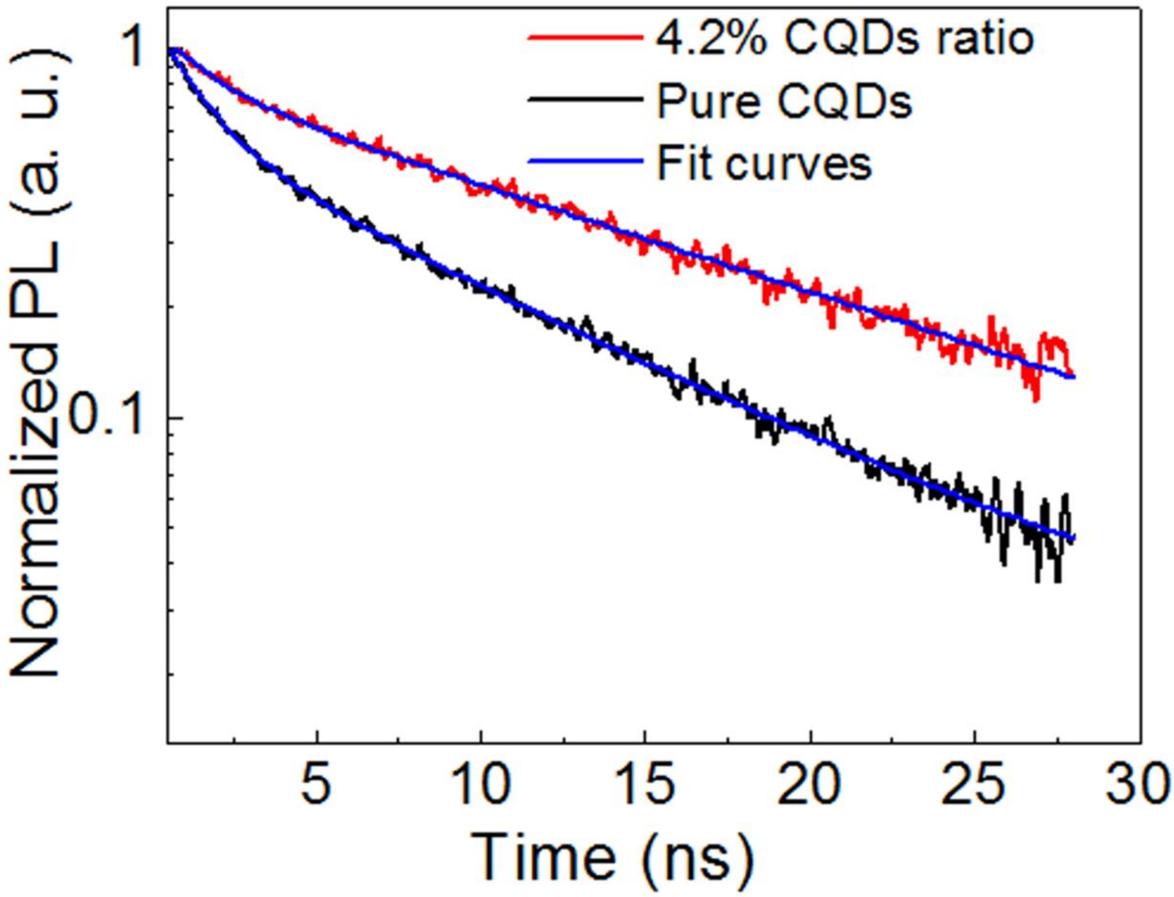

Supplementary Figure 8 Fitting of the TRPL decay curves of the pure CQD film and 4.2% volume ratio CQD-in-perovskite complex film.

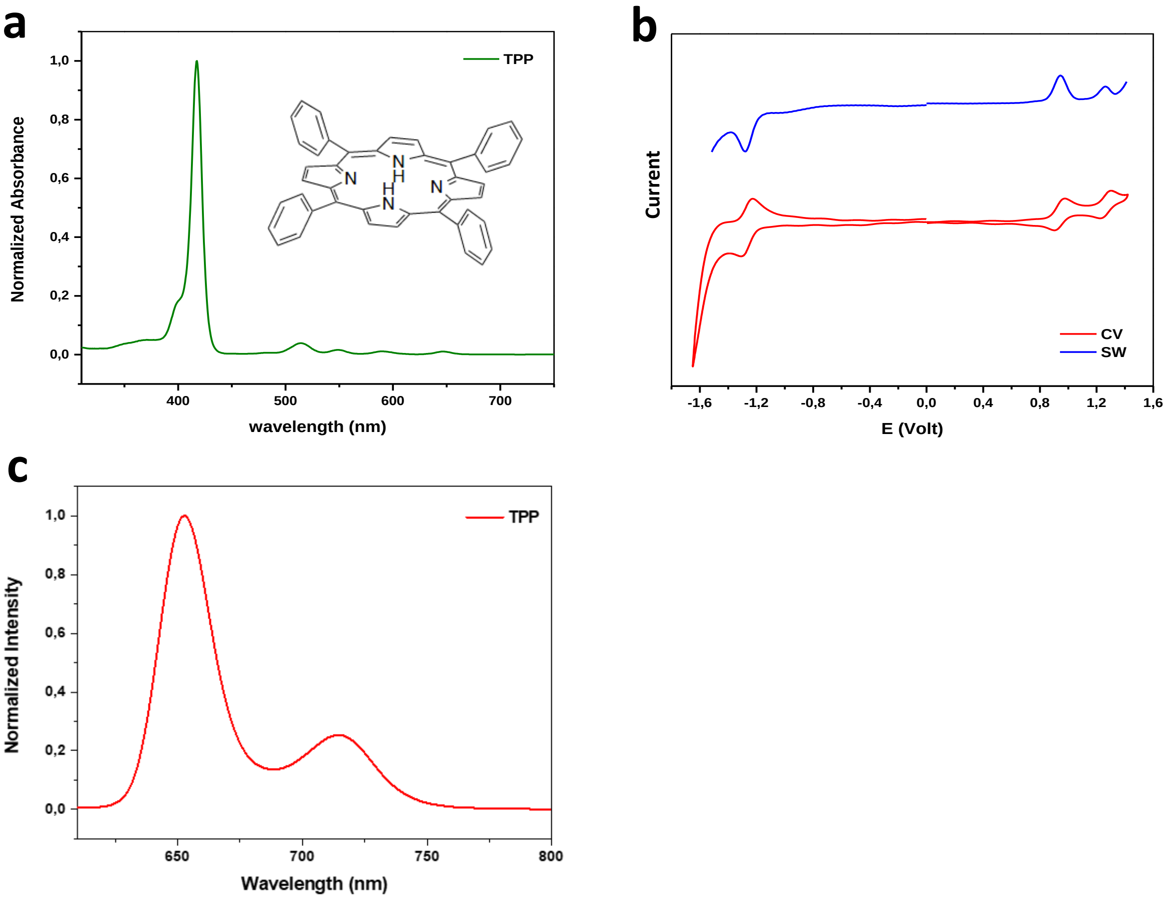

Supplementary Figure 9 Photophysical/optoelectronic properties of TPP porphyrin. a, Absorption spectrum of TPP in solution. (The chemical structure of TPP is shown in the inset.) **b**, Cyclic voltammetry (CV) and square wave (SW) measurements of porphyrin in DCM. All potentials are reported vs. SCE, and FcH/FcH^+ was used as the internal standard ($E^{ox}_{1/2}$ is 0.42 V). **c**, Room temperature emission spectrum of TPP in DCM when exciting the chromophore at 550 nm.

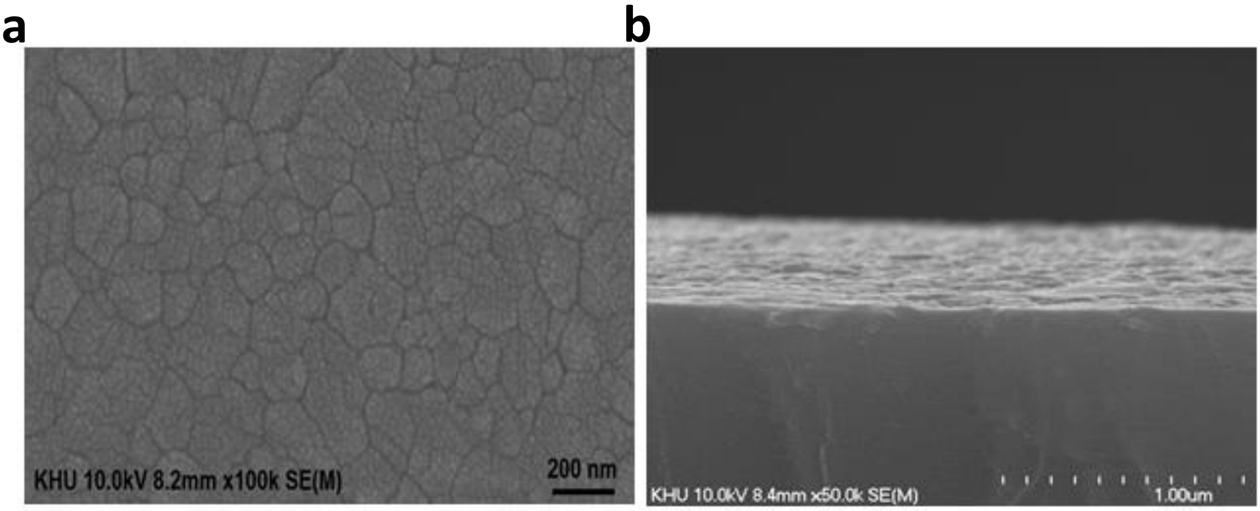

Supplementary Figure 10 Morphological properties of the thin films used in this study. a, Top view and **b**, cross-sectional view SEM images of CQDs in the triple cation perovskite deposited on an ITO/TiO_2 layer.

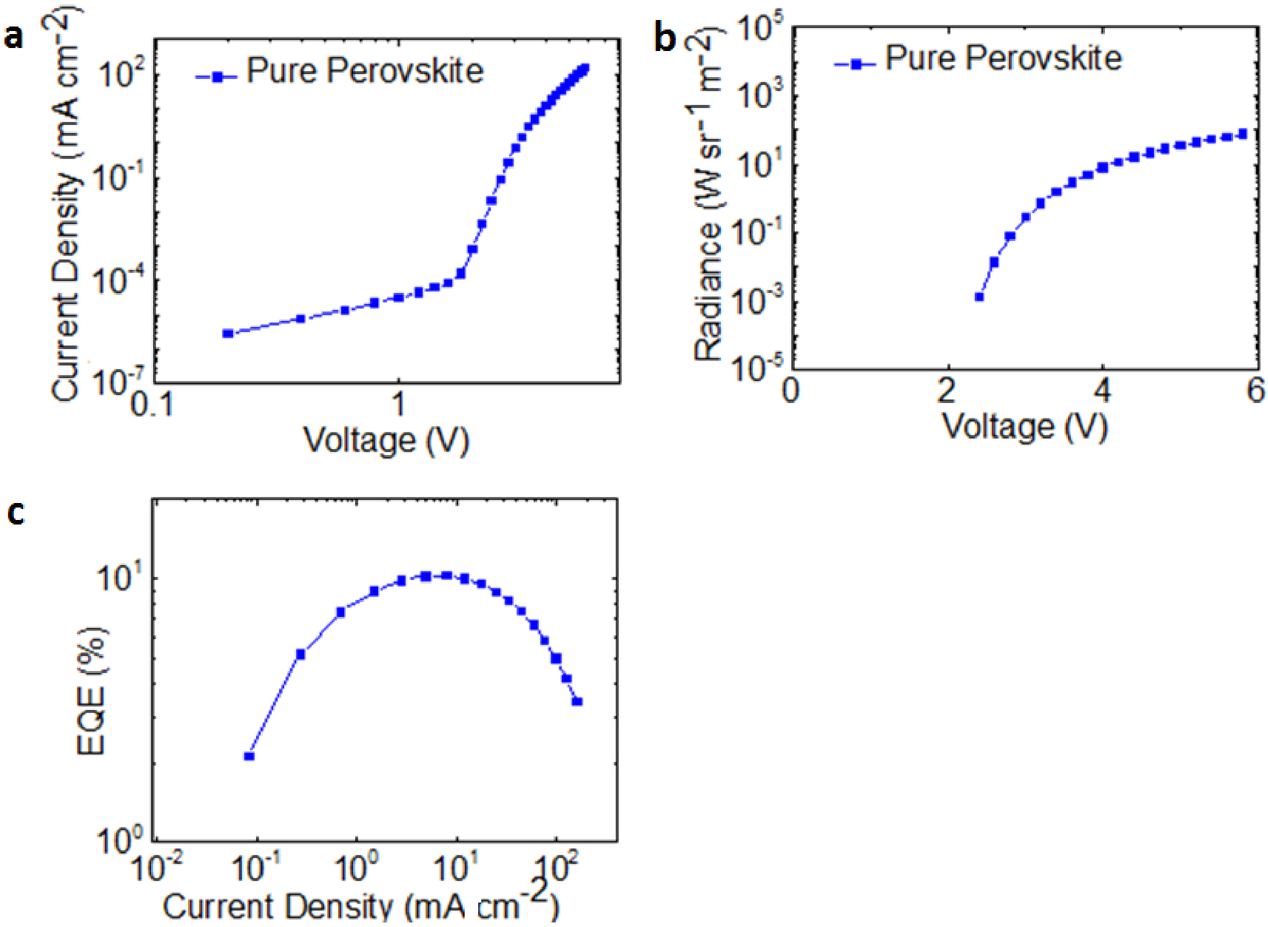

Supplementary Figure 11 Evaluation of the best-performing perovskite-only (iodine concentration of 80%) LEDs. a, Current density, **b**, radiance versus voltage, and **c**, EQE versus current density.

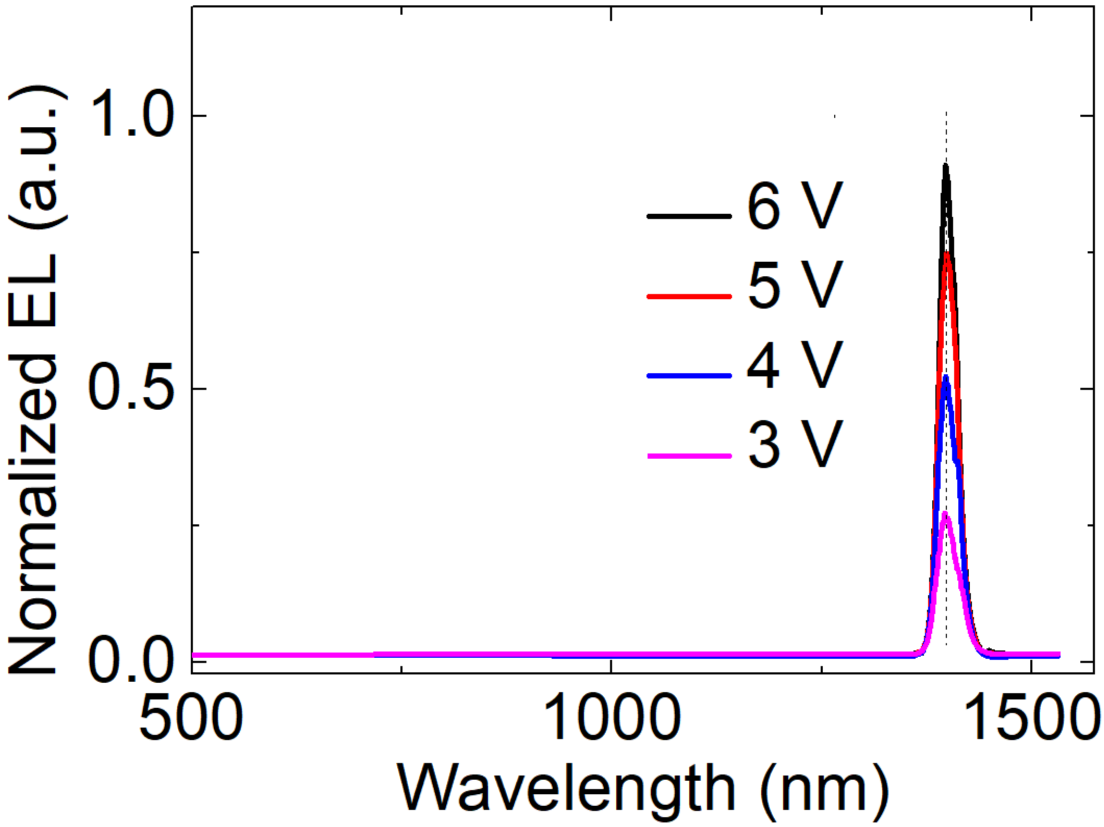

Supplementary Figure 12 Evolution of the EL spectra of CQD-in-triple-cation-perovskite LEDs with increasing voltage. As the perovskite emission (at approximately 750 nm) is not observed, we can conclude that injected electrons and holes are radiatively recombined and only photonic emission occurs within the CQD emitter.

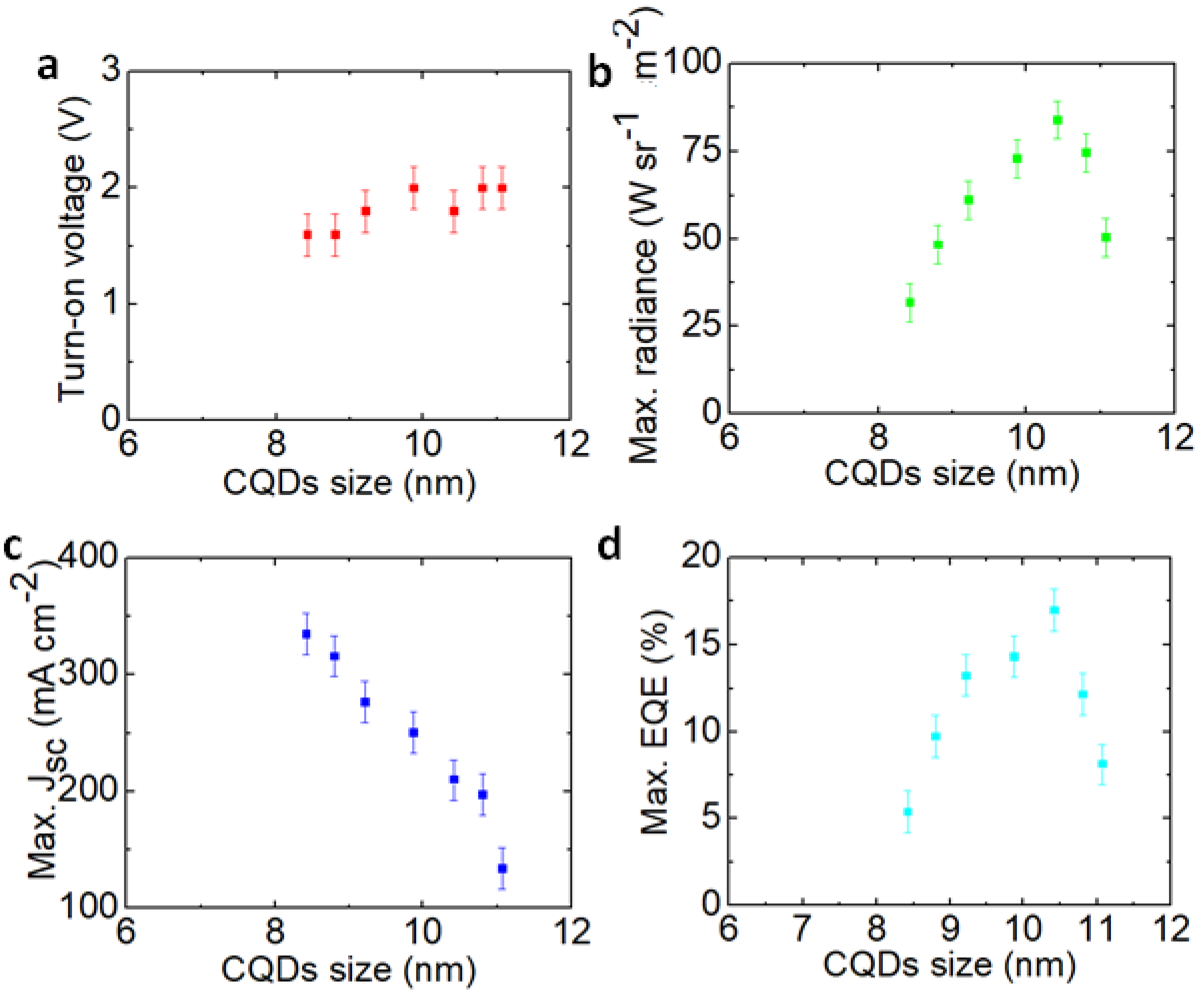

Supplementary Figure 13 NIR LED performance variation with CQD size. a, Turn-on voltage, **b,** maximum radiance, **c,** maximum current density, and **d,** peak EQE values of devices with various CQD sizes.

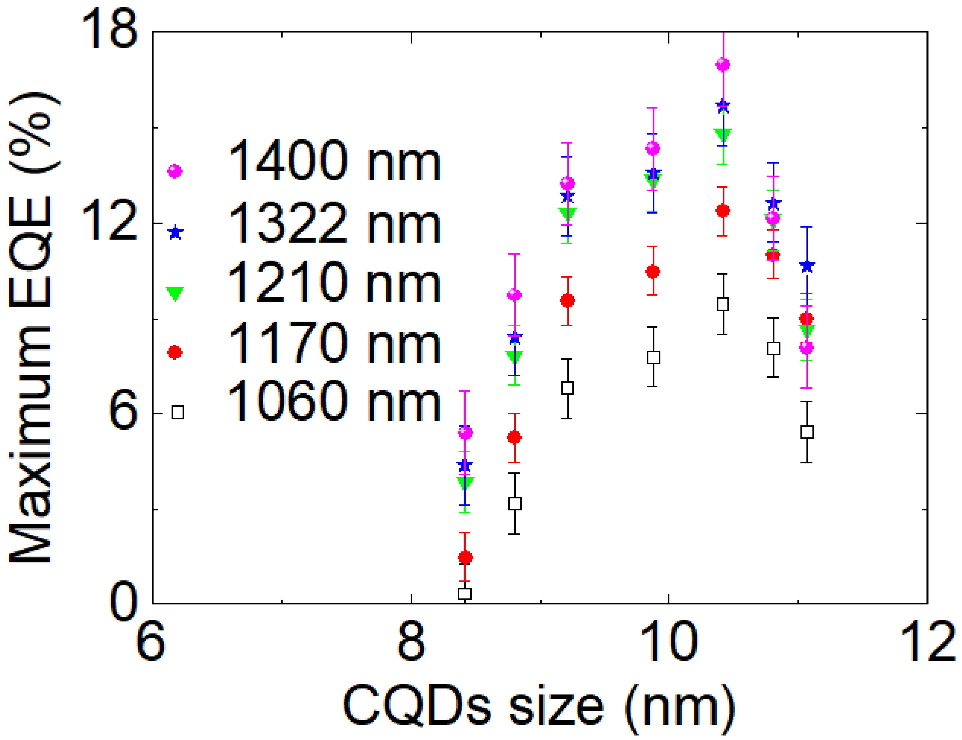

Supplementary Figure 14 Emission wavelength tunability of CQDs. Variation of the emission peak wavelength and maximum EQE with the CQD size.

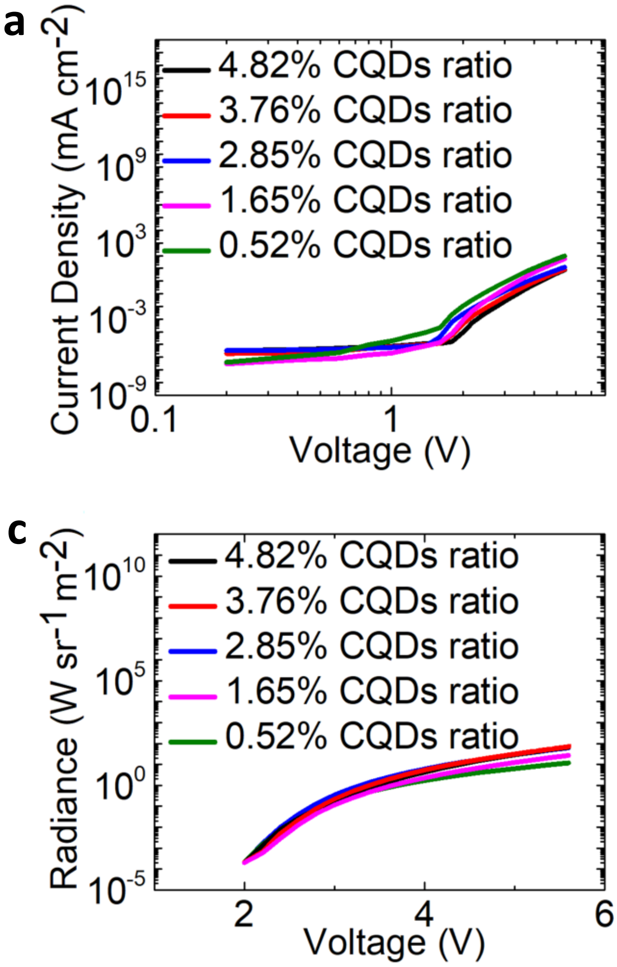

Supplementary Figure 15 Evolution of NIR LED performance with changing CQD content. Variation of the **a,** current density, **b,** EQE and **c,** radiance values of devices with CQD content.

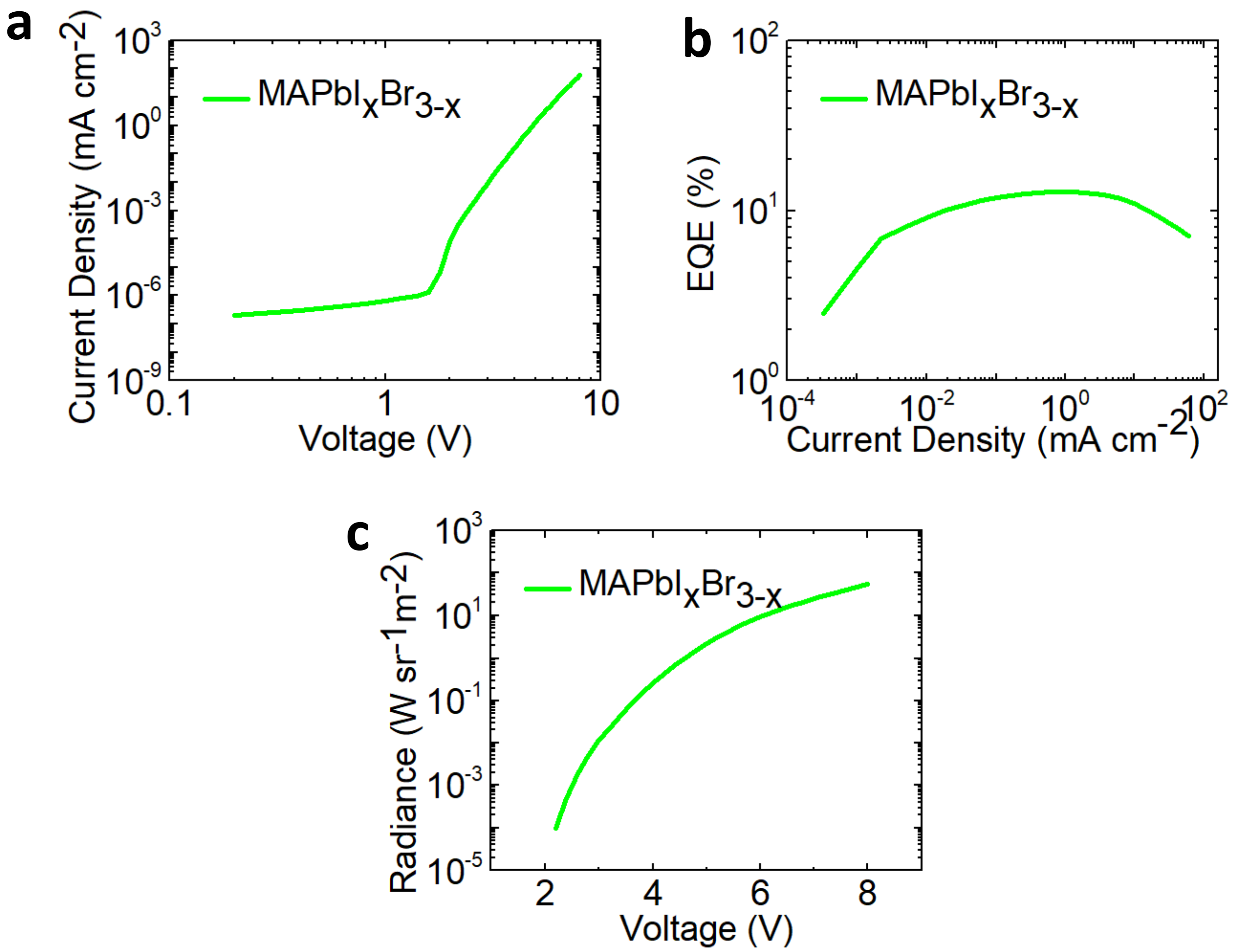

Supplementary Figure 16 Evaluation of LEDs based on $MAPbI_xBr_{3-x}$ as the host matrix. a, Current density versus voltage, **b**, EQE versus current density and **c**, radiance versus voltage of CQD NIR LEDs.

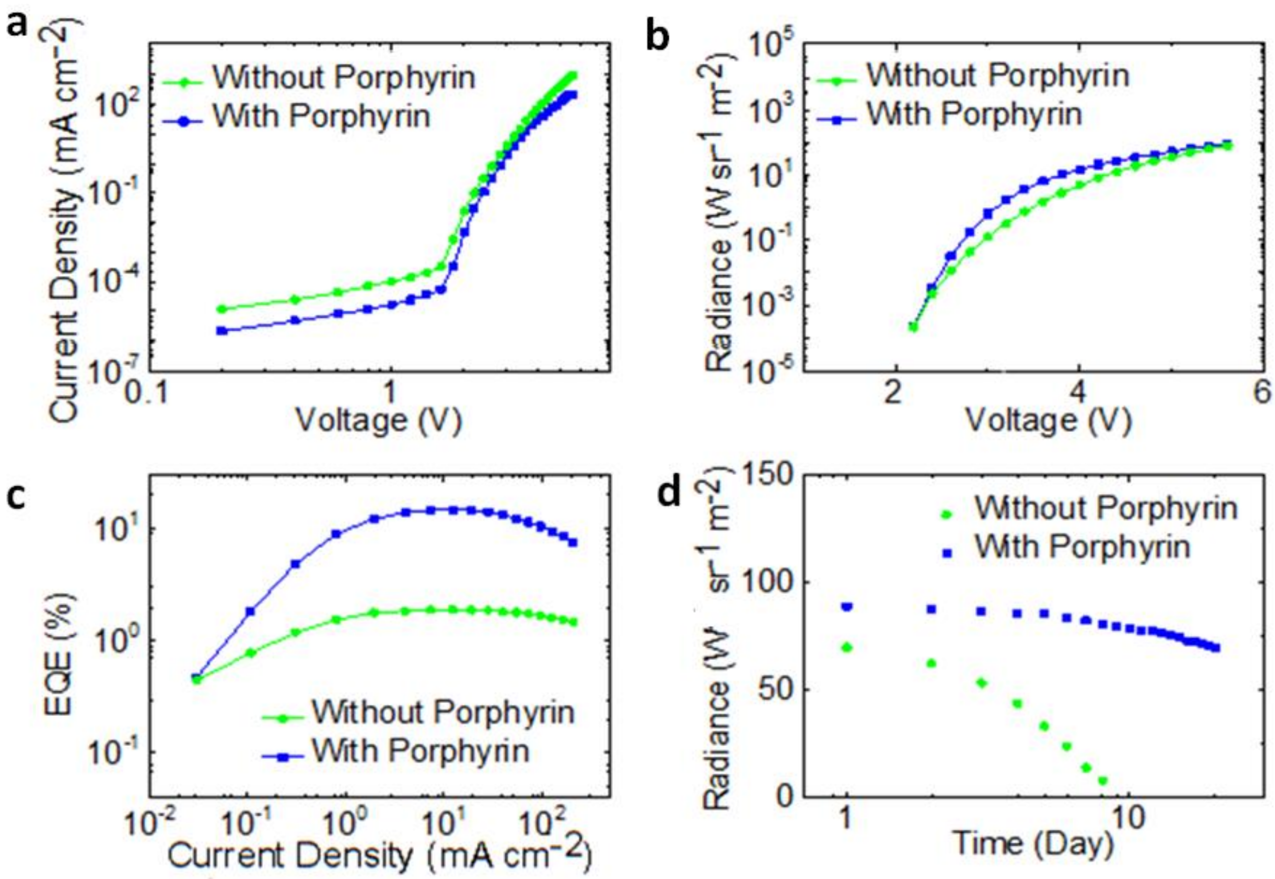

Supplementary Figure 17 Evaluation of LEDs with and without porphyrin. a, Current density versus voltage, **b**, radiance versus voltage, **c**, EQE versus current density and **d**, stability characteristics of CQD NIR LEDs.

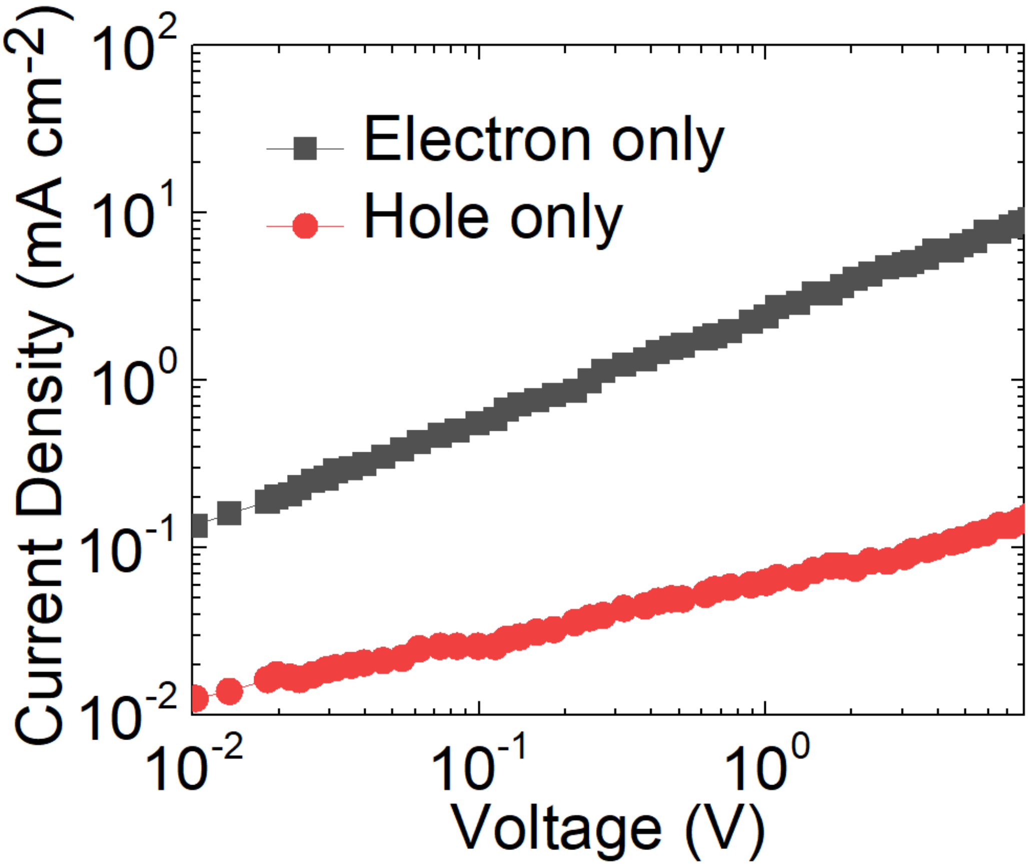

Supplementary Figure 18 Current density-voltage measurements on electron-only devices (ITO/TiO_2/CQDs+perovskite/Al) and hole-only devices without incorporation of a porphyrin interlayer at the perovskite/MoO_3 interface (ITO/CQDs+perovskite/MoO_3/Pd).

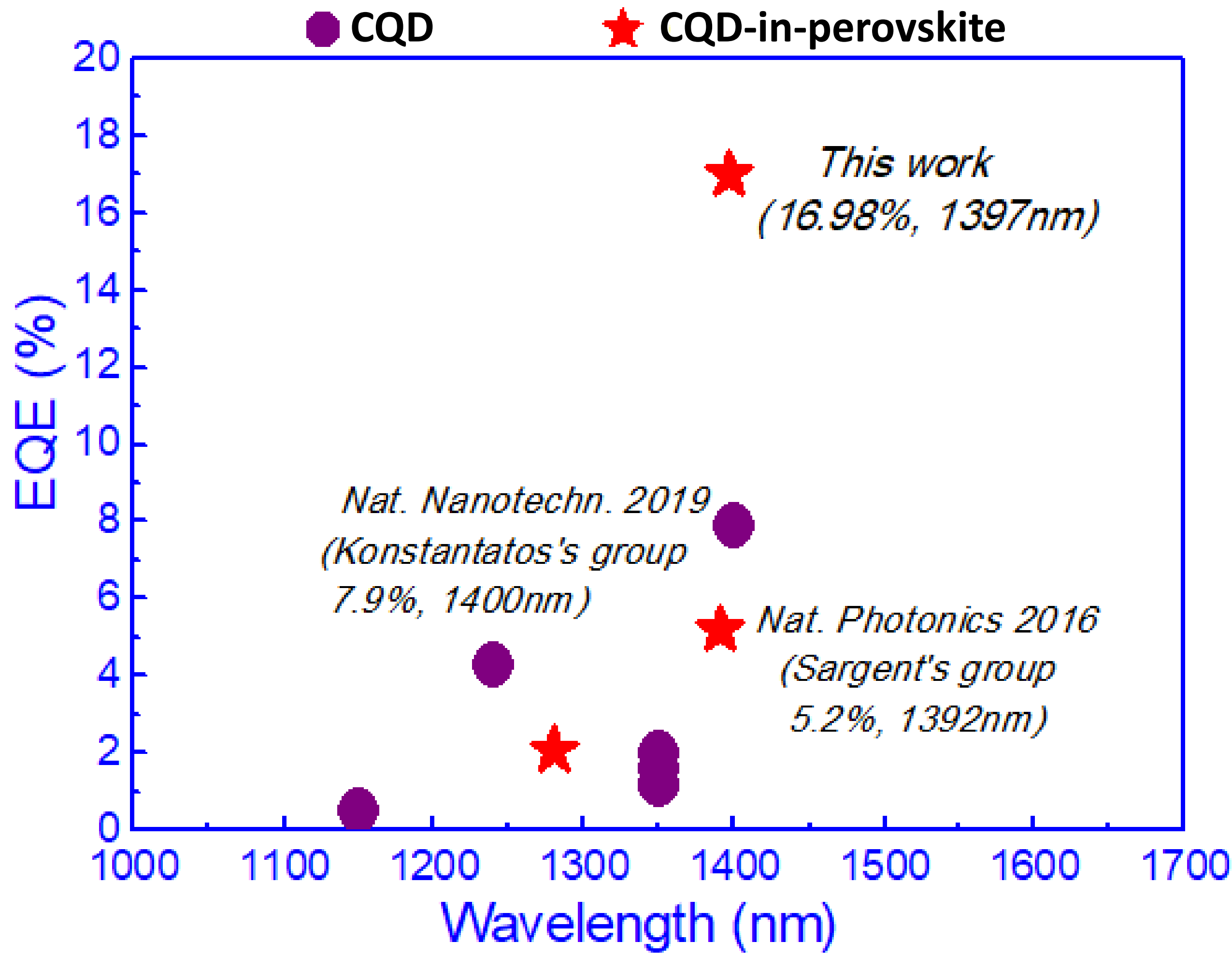

Supplementary Figure 19 Performance summary of the most efficient recently published solution-processed CQD LEDs emitting in the second NIR window[2-21].

Supplementary Tables

Supplementary Table 1 Optimization of the iodine concentration.

Iodine concentration	Peak EQE (%)
40	4.33
50	7.13
60	8.21
70	9.915
80	10.74
90	8.03
100	5.625

Supplementary Table 2 Emission and corresponding CQD sizes and PLQEs. The emission characteristics of $Ag_2S@SiO_2$ CQDs were measured using a 720 nm excitation wavelength.

Emission maximum (nm)	Size (nm)	PLQE (Φ)
1060	8.42±0.56	23%
1170	8.89±1.12	39%
1210	9.22±0.93	56%
1322	9.88±1.29	68%
1397	10.42±1.05	84%
1434	10.81±0.52	79%
1482	11.07±1.02	73%

Supplementary Table 3 TRPL results and fitting parameters for CQDs and CQD-in-perovskite films. (TRPL results were fitted to a two-exponential decay: $A_1\exp(-t/\tau_1)+A_2\exp(-t/\tau_2)$, where $A_1+A_2=1$.)

sample	A_1 (%)	τ_1 (ns)	A_2 (%)	τ_2 (ns)
Pure CQDs	44	1.55	56	10.69
4.2% CQD-in-perovskite	21	1.58	79	14.97

Supplementary Table 4 Summary of the performance parameters for NIR LEDs with increasing CQD size.

CQD size (nm)	Turn-on voltage (V)	Maximum radiance (W sr^{-1} m^{-2})	Maximum current density (mA cm^{-2})	Peak EQE (%)
8.42	1.6	31.77	335	5.38
8.89	1.6	48.43	316	9.75
9.22	1.8	61.10	277	13.23
9.88	2.1	72.86	251	14.33
10.42	1.6	83.93	210	16.98
10.81	2.0	74.57	197	12.15
11.07	2.0	50.44	134	8.11

Supplementary Table 5 Summary of the performance parameters for NIR LEDs with increasing CQD content within the perovskite matrix.

CQD content (%)	Turn-on voltage (V)	Maximum radiance (W sr^{-1} m^{-2})	Maximum current density (mA cm^{-2})	Peak EQE (%)
0.52	1.8	11.83	296.05	1.04
1.65	2.2	27.33	255.45	3.82
2.85	2.0	63.11	242.56	9.48
3.76	2.0	70.84	238.60	15.06
4.82	1.8	66.85	197.61	13.15

Supplementary Table 6 Summary of the performance parameters for NIR LEDs with the structure ITO/TiO_2/Ag_2S@SiO_2 added to $MAPbI_xBr_{3-x}$/porphyrin/MoO_3/Ag.

Device	Peak EL wavelength (nm)	Turn-on voltage (V)	Maximum radiance (W sr^{-1} m^{-2})	Maximum current density (mA cm^{-2})	Peak EQE (%)
4.2% CQD-in-perovskite	1397	2.2	54.25	60.94	12.96

Supplementary Table 7 Performance summary of recently published works on the most efficient solution-processed CQD NIR LEDs.

Peak EL wavelength (nm)	CQD	Turn-on voltage (V)	Maximum radiance (W sr^{-1} m^{-2})	Maximum current density (mA cm^{-2})	Peak EQE (%)	Year[Ref]
1000-1300	InAs	2.0	-	-	0.5	2002[5]
1200-1500	PbS	1.0	-	-	1.15	2008[6]
800	CdTe/CdSe	1.55	-	-	1.59	2013[7]
1350	PbS	1.2	0.29	0.1	1.6	2015[8]
950-1650	PbS	0.7-2.1	-	1000	2.0	2012[9]
1240	PbS-CdS	1.4	0.75	-	4.3	2015[10]
980	PbSe	-	-	-	5.3	2017[11]
853	Si	1.55	-	-	8.6	2011[12]
1400	PbS	0.6	9.00	1.75	7.9	2019[13]

Supplementary Table 8 Performance summary of recently published works on the most efficient solution-processed perovskite NIR LEDs.

EL wavelength (nm)	Emissive layer	Turn-on voltage (V)	Maximum radiance (W sr^{-1} m^{-2})	Maximum current density (mA cm^{-2})	Peak EQE (%)	Year[Ref]
760-770	$CH_3NH_3PbI_{3-x}Cl_x$	1.3	28	160	3.5	2015[14]
950	$CsSnI_3$	1.5-2.0	40	364.3	3.8	2016[15]
750-800	$FAPbI_3$	-	206.7	1000	5.5	2018[16]
750	$PEA_2(MA)_{n-1}Pb_nI_{3n+1}$	3.8	80	64	8.8	2016[17]
750	$Cs_{10}(MA_{0.17}FA_{0.83})Pb(Br_xI_{1-x})_3$	2.8	93.34	286.14	9.23	2017[6]
748	$(BAI)_{0.2}MAPbI_3$	-	30	-	10.4	2017[18]
763	$NFPI_6B$	1.3	82	100	11.7	2016[19]
780	$NFPI_7$	1.5	-	500	12.7	2018[20]
803	$5AVA/FAI/PbI_2$	1.25	390	18	20.7	2018[21]
800	$FAPbI_3$	1.25	308	200	21.6	2019[22]

Supplementary Table 9 Performance summary of recently published works on the most efficient solution-processed CQD-in-perovskite NIR LEDs.

EL wavelength (nm)	Emissive layer	Turn-on voltage (V)	Maximum radiance (W sr^{-1} m^{-2})	Maximum current density (mA cm^{-2})	Peak EQE (%)	Year[Ref]
1280	PbS in $(BA)_2PbI_4$	1.1	1.5	-	2.06	2017[23]
1391	PbS in $MAPb_xBr_{3-x}$	<1	2.6	-	5.2	2016[24]
1397	$Ag_2S@SiO_2$ in triple cation perovskite	1.6	83.93	210	16.98	This work

Supplementary Table 10 Performance summary of solution-processed NIR OLEDs with record efficiencies.

EL wavelength (nm)	Emissive layer	Turn-on voltage (V)	Maximum radiance (W sr^{-1} m^{-2})	Maximum current density (mA cm^{-2})	Peak EQE (%)	Year[Ref]
721	boron difluoride curcuminoid in CBP	-	500	-	10	2018[25]

References

1. Jiang, W. et al. Photocatalytic performance of Ag_2S under irradiation with visible and near-infrared light and its mechanism of degradation. *RSC Adv*. **5**, 24064–24071 (2015).
2. Liu, M. et al. Aluminum-doped caesium lead bromide perovskite nanocrystals with stable blue photoluminescence used for display backlight. *Advanced Science* **4**(11), 1700335 (2017).
3. Saliba, M. et al. Caesium-containing triple cation perovskite solar cells: improved stability, reproducibility and high efficiency. *Energy Environ. Sci.* **9**, 1989–1997 (2016).
4. Du, Y. et al. Near-infrared photoluminescent Ag_2S quantum dots from a single source precursor. *J. Am. Chem. Soc.* **132** (5), 1470–1471 (2010).
5. Tessler, N., Medvedev, V., Kazes, M., Kan, S. & Banin, U. Efficient near-infrared polymer nanocrystal light-emitting diodes, *Science* **295,** 1506–1508 (2002).
6. Bourdakos, K. N., Dissanayake, D. M. N. M., Lutz, T., Silva, S. R. P. & Curry, R. J. Highly efficient near-infrared hybrid organic-inorganic nanocrystal electroluminescence device. *Appl. Phys. Lett* .**92,** 153311 (2008).
7. Shen, H. et al. Highly efficient near-infrared light-emitting diodes by using type-II CdTe/CdSe core/shell quantum dots as a phosphor, *Nanotechnology* **24**, 475603 (2013).
8. Yang, Z. et al. All-quantum-dot infrared light-emitting diodes. *ACS Nano* **9** (12), 12327–12333 (2015).

9. Sun, L., et al. Bright infrared quantum-dot light-emitting diodes through inter-dot spacing control. *Nat. Nanotechnol.* **7,** 369–373 (2012).

10. Supran, G.J. et al. High-performance shortwave-infrared light-emitting devices using core–shell (PbS–CdS) colloidal quantum dots, *Adv. Mater*. **27**, 1437–1442 (2015).

11. Wang, Y. et al. Efficient near-infrared light-emitting diodes based on liquid PbSe quantum dots. *Nanotechnology* **28**, 215703 (2017).

12. Cheng, K.-Y., Anthony, R., Kortshagen, U. R. & Holmes, R. J. High-Efficiency Silicon Nanocrystal Light-Emitting Devices. *Nano Lett.* **11** (5), 1952–1956 (2011).

13. Pradhan, S. et al. High-efficiency colloidal quantum dot infrared light-emitting diodes via engineering at the supra-nanocrystalline level, *Nat. Nanotechnol.* **14**, 72–79 (2019).

14. Wang, J. et al. Interfacial control toward efficient and low-voltage perovskite light-emitting diodes. *Adv. Mater.* **27**(14), 2311–2316 (2015).

15. Hong, W.-L. et al. Efficient low-temperature solution processed lead-free perovskite infrared light-emitting diodes. *Adv. Mater*. **28**, 8029–8036 (2016).

16. Giuri, A. et al. Ultra-bright near-infrared perovskite light-emitting diodes with reduced efficiency roll-off. *Scientific Reports* **8**, 15496 (2018).

17. Yuan, M. et al. Perovskite energy funnels for efficient light-emitting diodes. *Nat. Nanotechnol*. **11**, 872–877 (2016).

18. Xiao, Z. et al. Efficient perovskite light-emitting diodes featuring nanometre-sized crystallites. *Nat. Photonics* **11**, 108 (2017).

19. Wang, N. et al. Perovskite light-emitting diodes based on solution-processed self-organized multiple quantum wells. *Nature Photonics* **10** (11), 699–704 (2016).

20. Zou, W. et al. Minimising efficiency roll-off in high-brightness perovskite light-emitting diodes. *Nat Commun.* **9**, 608 (2018).

21. Cao, Y. et al. Perovskite light-emitting diodes based on spontaneously formed submicrometre-scale structures. *Nature* **562**, 249–253 (2018).

22. Xu, W. et. al. Rational molecular passivation for high performance perovskite light-emitting diodes. *Nature Photonics* **13**, 418–424 (2019).

23. Yang, Z. et al. Quantum dots in two-dimensional perovskite matrices for efficient near-Infrared light emission. *ACS Photonics* **4**, 830−836 (2018).

24. Gong, X. et al. Highly efficient quantum dot near-infrared light-emitting diodes. *Nature Photonics* **10**, 253−257 (2016).

25. Kim, D.-H. et al. High-efficiency electroluminescence and amplified spontaneous emission from a thermally activated delayed fluorescent near-infrared emitter. *Nature Photonics* **12**, 98−104 (2018).